

Provided for non-commercial research and education use.
Not for reproduction, distribution or commercial use.



This article appeared in a journal published by Elsevier. The attached copy is furnished to the author for internal non-commercial research and education use, including for instruction at the authors institution and sharing with colleagues.

Other uses, including reproduction and distribution, or selling or licensing copies, or posting to personal, institutional or third party websites are prohibited.

In most cases authors are permitted to post their version of the article (e.g. in Word or Tex form) to their personal website or institutional repository. Authors requiring further information regarding Elsevier's archiving and manuscript policies are encouraged to visit:

<http://www.elsevier.com/copyright>



Contents lists available at ScienceDirect

Journal of Non-Newtonian Fluid Mechanics

journal homepage: www.elsevier.com/locate/jnnfm

Influence of viscoelasticity on drop deformation and orientation in shear flow Part 1. Stationary states

Kristof Verhulst^a, Ruth Cardinaels^a, Paula Moldenaers^a, Yuriko Renardy^{b,*}, Shahriar Afkhami^b

^a Katholieke Universiteit Leuven, Department of Chemical Engineering, W. de Croylaan 46 - B 3001 Heverlee, Leuven, Belgium

^b Department of Mathematics and ICAM, 460 McBryde Hall, Virginia Polytechnic Institute and State University, Blacksburg VA 24061-0123, USA

ARTICLE INFO

Article history:

Received 28 September 2007

Received in revised form 10 June 2008

Accepted 11 June 2008

Keywords:

Drop deformation

Oldroyd-B model

Volume-of-fluid method

Blend morphology

Viscoelasticity

ABSTRACT

The influence of matrix and droplet viscoelasticity on the steady deformation and orientation of a single droplet subjected to simple shear is investigated microscopically. Experimental data are obtained in the velocity–vorticity and velocity–velocity gradient plane. A constant viscosity Boger fluid is used, as well as a shear-thinning viscoelastic fluid. These materials are described by means of an Oldroyd-B, Giesekus, Ellis, or multi-mode Giesekus constitutive equation. The drop-to-matrix viscosity ratio is 1.5. The numerical simulations in 3D are performed with a volume-of-fluid algorithm and focus on capillary numbers 0.15 and 0.35. In the case of a viscoelastic matrix, viscoelastic stress fields, computed at varying Deborah numbers, show maxima slightly above the drop tip at the back and below the tip at the front. At both capillary numbers, the simulations with the Oldroyd-B constitutive equation predict the experimentally observed phenomena that matrix viscoelasticity significantly suppresses droplet deformation and promotes droplet orientation. These two effects saturate experimentally at high Deborah numbers. Experimentally, the high Deborah numbers are achieved by decreasing the droplet radius with other parameters unchanged. At the higher capillary and Deborah numbers, the use of the Giesekus model with a small amount of shear-thinning dampens the stationary state deformation slightly and increases the angle of orientation. Droplet viscoelasticity on the other hand hardly affects the steady droplet deformation and orientation, both experimentally and numerically, even at moderate to high capillary and Deborah numbers.

© 2008 Elsevier B.V. All rights reserved.

1. Introduction

Dilute polymeric blends commonly form a droplet–matrix interface [1,2]. The final material properties are significantly influenced by the deformation, break-up and coalescence of droplets during flow. Control of these processes is therefore essential in the development of high performance blends. The investigation of single droplet dynamics in simple shear is a contribution towards this goal. In fact, theoretical and experimental studies on the single droplet problem recently include the effects of component viscoelasticity [3]. Perturbation theories for small deformation [4,5] predict that viscoelasticity hardly affects the steady droplet deformation at low flow intensity. Steady droplet orientation towards the (shear) flow direction is predicted to be highly promoted by matrix viscoelasticity. The effect of droplet viscoelasticity on the orientation of the droplet is less pronounced. Several experimental studies confirm these trends [6–8].

The small deformation theories are modified and extended to handle larger droplet deformations in recent phenomenological models. In the case of steady droplet deformation, quantitative agreement is found for low to moderate droplet deformations. At high droplet deformations, the discrepancy with experimental results is more pronounced. [8–14].

In planar extensional flow [15] and uniaxial elongational flow [16], matrix elasticity promotes droplet deformation at stationary states for viscosity ratios ($\lambda =$ drop to matrix ratio) less than or equal to one. In the case of droplet elasticity, the opposite is found [16,17]. For $\lambda > 1$, experiments on planar extensional flow with various non-Newtonian droplet systems result in stationary shapes that resemble corresponding Newtonian–Newtonian systems [18]. Less attention has been given to the study of simple shear. Experimental results of Guido et al. [7] demonstrate that matrix viscoelasticity suppresses droplet deformation at high flow intensities at viscosity ratios 0.1, 1 and 4.7. This result is confirmed by Verhulst et al. [8] at viscosity ratio 0.75 and is in qualitative agreement with the predictions of the phenomenological models [9–11]. On the contrary, several authors conclude the opposite, i.e. matrix elasticity enhances droplet deformation [19–21]. The numerical investigation of Yue et al. [22] clarifies the interaction

* Corresponding author.

E-mail address: renardyy@aol.com (Y. Renardy).

between the various stress components and pressure acting on the surface of the droplet, and explains the differences according to the level of matrix elasticity. In addition, Verhulst et al. [8] demonstrate that similar materials, studied at moderate to high shear rates, can yield different steady droplet deformations under the same experimental conditions; i.e. when the same dimensionless parameters (borrowed from small deformation theory) are studied for different materials.

Experimental studies on the deformation of a viscoelastic droplet in a Newtonian matrix have only been performed at a viscosity ratio of one in the papers of Lerdwijitjarud et al. [23,24] and Sibillo et al. [13]. In the latter, the experimental results are compared with a model equation. Numerical simulations are conducted in [25] for an Oldroyd-B droplet in a Newtonian matrix under simple shear. The drop is found to deform less as the Deborah number increases, while at high capillary numbers, the deformation increases with increasing Deborah number. A first-order ordinary differential equation is used as a phenomenological model [25]. It describes an overdamped system, in which the viscous stretching force is proportional to the shear rate, a damping term is proportional to viscosity, and a restoring force is proportional to the first normal stress difference. The latter creates an elastic force which acts to eventually decrease deformation, but it predicts greater decrease than observed in the numerical results. Moreover, the model cannot predict the critical curve in the Ca vs. λ parameters for the Stokes regime, nor the transient overshoot which results from strong initial conditions [26], or predict results for a Newtonian drop in a viscoelastic matrix. The suppression of deformation with increasing drop elasticity is also noted in the theoretical and numerical studies of [9,22,27,28].

In this paper, the influence of both matrix and droplet viscoelasticity on the steady deformation and orientation of a single droplet subjected to a homogeneous shear flow is investigated at a viscosity ratio of 1.5. The study is performed for a broad range of the relevant dimensionless parameters, which allows the examination of the dependence on matrix elasticity in 3D at high Deborah numbers. The 2D study of [22] finds a numerically small non-monotonic dependence of stationary state deformation on the matrix Deborah number, which is not noticeable in 3D for the specific parameters of this study. Throughout this paper, the experimental results are compared with three-dimensional simulations performed with a volume-of-fluid algorithm for viscoelastic liquid–liquid systems.

2. Numerical simulations

The governing equations are as follows. The liquids are density-matched. For each liquid, the solvent viscosity is denoted η_s , polymeric viscosity η_p , total viscosity $\eta = \eta_s + \eta_p$, relaxation time τ , shear rate $\dot{\gamma}$, and the initial elastic modulus $G(0) = \eta_p/\tau$. Additional subscripts 'd' and 'm' denote the drop and matrix liquids. The governing equations include incompressibility and momentum transport:

$$\begin{aligned} \nabla \cdot \mathbf{u} &= 0, \\ \rho \left(\frac{\partial \mathbf{u}}{\partial t} + \mathbf{u} \cdot \nabla \mathbf{u} \right) &= \nabla \cdot \mathbf{T} - \nabla p + \nabla \cdot (\eta_s (\nabla \mathbf{u} + (\nabla \mathbf{u})^T)) + \mathbf{F}, \end{aligned} \quad (1)$$

where \mathbf{T} denotes the extra stress tensor. The total stress tensor is $\boldsymbol{\tau} = -p\mathbf{I} + \mathbf{T} + \eta_s[\nabla \mathbf{u} + (\nabla \mathbf{u})^T]$. Each liquid is identified with a color function,

$$C(\mathbf{x}, t) = \begin{cases} 0 & \text{in the matrix liquid} \\ 1 & \text{in the drop} \end{cases} \quad (2)$$

which advects with the flow. The position of the interface is given by the discontinuities in the color function. The interfacial tension

force is formulated as a body force

$$\mathbf{F} = \Gamma \tilde{\kappa} \mathbf{n} \delta_S, \quad \tilde{\kappa} = -\nabla \cdot \mathbf{n}, \quad (3)$$

where Γ denotes the surface tension, \mathbf{n} the normal to the interface, δ_S the delta-function at the interface, and $\tilde{\kappa}$ the curvature. In (3), $\mathbf{n} = \nabla C/|\nabla C|$, $\delta_S = |\nabla C|$.

The drop and matrix liquids are governed by the Giesekus constitutive equations, which has had reasonable success in comparisons of two-layer channel flow with actual data [29]. One feature that distinguishes the Giesekus model from others is the non-zero second normal stress difference N_2 . This is relevant to the flow of two immiscible liquids because it has been shown that a discontinuity in N_2 affects interfacial stability [30]. In one limit, the Giesekus model reduces to the simpler Oldroyd-B constitutive equation. The experimental data which are addressed in this paper are as a first approximation, Oldroyd-B liquids [8]. However, the Oldroyd-B model is a difficult one to implement because it overpredicts the growth of stresses at large deformation rates and lead to numerical instability. The Giesekus constitutive equation is

$$\begin{aligned} \tau \left(\frac{\partial \mathbf{T}}{\partial t} + (\mathbf{u} \cdot \nabla) \mathbf{T} - (\nabla \mathbf{u}) \mathbf{T} - \mathbf{T} (\nabla \mathbf{u})^T \right) &+ \mathbf{T} + \tau \kappa \mathbf{T}^2 \\ &= \tau G(0) (\nabla \mathbf{u} + (\nabla \mathbf{u})^T). \end{aligned} \quad (4)$$

The dimensionless parameters are the viscosity ratio (based on total viscosities) $\lambda = \eta_d/\eta_m$, $Ca = R_0 \dot{\gamma} \eta_m / \Gamma$, a Weissenberg number per fluid $We = \dot{\gamma} \tau$, and retardation parameter per fluid $\beta = \eta_s/\eta$. A Reynolds number based on the matrix liquid $Re = \rho \dot{\gamma} R_0^2 / \eta_m$ is in the range .01–.05, chosen small so that inertia is negligible.

Alternatively, let Ψ_1 denote the first normal stress coefficient, equivalent to $2\eta_p \tau$, and define the Deborah number by

$$\tilde{De} = \frac{\Psi_1 \Gamma}{2R_0 \eta^2}; \quad (5)$$

i.e., $\tilde{De}_d = (1 - \beta_d) We / (\lambda Ca)$, and $\tilde{De}_m = (1 - \beta_m) We / Ca$. Numerical and experimental results in later sections are presented in terms of the Deborah numbers, and dimensionless capillary time

$$\frac{t\Gamma}{\eta_m R_0} = \frac{t\dot{\gamma}}{Ca}, \quad (6)$$

hereinafter denoted \hat{t} . The rescaled Giesekus parameter

$$\tau \kappa G(0) \quad (7)$$

is relabeled $\hat{\kappa}$. The physically viable range is $0 \leq \hat{\kappa} < 0.5$ [30]. The Oldroyd-B model is $\hat{\kappa} = 0$.

The governing equations are discretized with the volume-of-fluid (VOF) method given in Ref. [26]. The interfacial tension force (3) is approximated by either the continuum surface force formulation (CSF) or the parabolic representation of the interface for the surface tension force (PROST). The reader is referred to Refs. [31,32,28] for these algorithms. Both VOF-PROST and VOF-CSF codes are parallelized with OpenMP. The efficiency of the parallelization for the Newtonian part of the code is discussed in [33]; the viscoelastic part has analogous properties. A typical computation presented in this paper is $\Delta x = R_0/16$, $\Delta \hat{t} = 0.00005/Ca$, $L_x = 16R_0$, $L_y = 8R_0$, $L_z = 8R_0$, for which one timestep takes 1.2 s with 64 processors on the SGI Altix 3700 supercluster at Virginia Tech. A simulation from dimensionless capillary time 0–11, with 64 nodes takes roughly 25 h.

2.1. Boundary conditions

The computational domain is denoted $0 \leq x \leq L_x$, $0 \leq y \leq L_y$, $0 \leq z \leq L_z$. The boundaries at $z = 0, L_z$ are walls which move

Table 1
Blend characteristics at experimental conditions

	Droplet–matrix	Droplet phase	Matrix phase	Temperature (°C)	Γ (mN/m)	λ
1	VE–NE	BF2	Saturated Rhodorsil	26.00±0.10	2.2 ±0.1	1.5
2	VE–NE	BR16	Infineum mix	24.45 ±0.03	2.65 ±0.05	1.5
3	NE–VE	Rhodorsil mix 1	BF2	26.40 ±0.04	2.0 ±0.1	1.5
4	NE–NE	Rhodorsil mix 2	Parapol 1300	25.50 ±0.05	2.7 ±0.1	1.5

with speeds $\pm U_0$. This results in the velocity field $(U(z), 0, 0)$ in the absence of the drop, where $U(z) = U_0(2z - L_z)/L_z$. The shear rate is $\dot{\gamma} = U'(z) = 2U_0/L_z$. Spatial periodicity is imposed in the x and y directions, at $x = 0, L_x$ and $y = 0, L_y$, respectively. Additional boundary conditions are not needed for the extra stress components. For computational efficiency, L_x, L_y and L_z are chosen to minimize the effect of neighboring drops and that of the walls. Typically, the distance between the walls is eight times the drop radius, as is the spanwise period, and the period in the flow direction is chosen dependent on drop extension. In these and prior (Newtonian) simulations, the influence of the boundaries is negligible under these circumstances. Experimental results on the effect of confinement are consistent with this [34].

2.2. Initial conditions

The drop is initially spherical with radius R_0 . The top and bottom walls are impulsively set into motion from rest. This requires that the viscoelastic stress tensor and velocity are initially zero. Since the velocity field is essentially governed by a parabolic PDE close to Stokes flow, the velocity adjusts immediately to simple shear so that whether the initial velocity field is zero or simple shear makes no difference in the numerical simulations. The initial viscoelastic stress values do, on the other hand, influence drop deformation. For example, if the drop were placed in a pre-existing shear flow, the initial viscoelastic stress is equal to the values which would prevail in the corresponding simple shear flow with the given shear rate. Fig. 4 of [26] shows that a drop placed in an already established flow immediately experiences a large viscoelastic stress and the deformation may overshoot. On the other hand, if the matrix fluid is viscoelastic with zero initial viscoelastic stress, then even with an established velocity field, it starts out with lower viscous stress due to the absence of polymer viscosity. This lowers the magnitude of stress in the matrix fluid, which pulls the drop more gently.

2.3. Drop diagnostics

We report the drop diagnostics with the same notation as in [8,35]. The slice through the center in the x – z plane, or the velocity–velocity gradient plane, provides the drop length L and breadth B . The angle of inclination to the flow direction is denoted θ . When viewed from above the drop, the slice through the center of the drop in the x – y plane, or the velocity–vorticity plane, gives the drop width W and length L_p . The Taylor deformation parameters are $D = (L - B)/(L + B)$ and $D_p = (L_p - W)/(L_p + W)$. The viscoelastic stress fields displayed in this paper are generated from contour values of the trace of the extra stress tensor, $\text{tr}(\mathbf{T})$. This is directly proportional to the extension of the polymer molecules, and is meaningful to plot from the direct numerical simulations. Contour values are given on the numerical plots in order to provide a comparison among the plots.

2.4. Accuracy

Computational accuracy for the Oldroyd-B portion is discussed in [28] for the 2D code, and in [26] for the 3D version. Fig. 1 is a

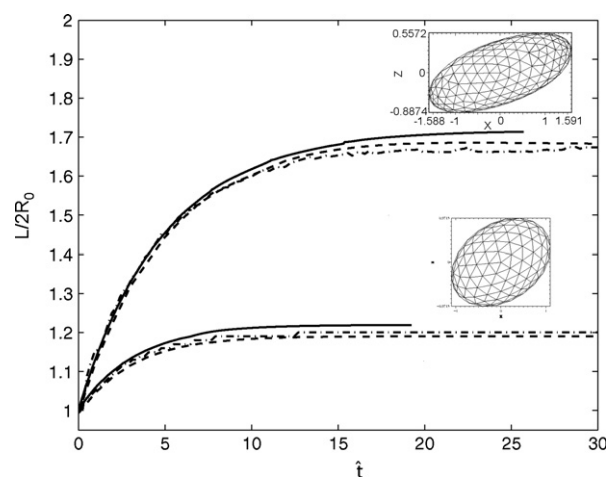


Fig. 1. Newtonian reference system with viscosity ratio 1.5 (system 4 of Table 1). Experimental data (---) at $Ca = 0.156$ (lower), 0.363 (upper) are compared with numerical simulations with the boundary integral code of [36](-.-) and VOF-CSF (—).

comparison of the experimental data (---) on the sideview length for the Newtonian reference system 4 of Table 1. Two numerical methods, the VOF-CSF (—) and the boundary integral scheme of Ref. [36], are used to provide quantitative agreement.

Tests for convergence with spatial and temporal refinements are performed to decide on optimal meshing. Table 2 shows deformation and angle of inclination for an Oldroyd-B drop in Newtonian matrix with the CSF formulation at $Ca = 0.35, \tilde{D}e_d = 2.6, \lambda = 1.5$ and $Re = 0.05$. The computational box is $L_x = 16R_0, L_y = 8R_0, L_z = 8R_0$. The results are also close for the PROST algorithm; since PROST is more CPU intensive, CSF is used for later results.

Fig. 2 shows contours of trace (\mathbf{T}) computed for the vertical cross-section through the center of a Oldroyd-B drop. The first row is $\hat{t} = 5$, the second row is $\hat{t} = 10$ and the third is $\hat{t} = 15$. With $\Delta t \dot{\gamma} = 0.0001$, the mesh is varied from $\Delta x = R_0/8$ for the first column, $\Delta x = R_0/12$ for the middle column and $R_0/16$ for the third column. The middle column is chosen as optimal: $\Delta x = R_0/12$ for $Ca = 0.35, \tilde{D}e_d = 2.6, \lambda = 1.5$. The temporal mesh is also varied to optimize the timestep. The stresses vary steeply close to the interface and the contours are constructed from an interpolation of the values from the simulations. This procedure may contribute to some inaccuracy in the shape of the contours, and also that they cross the interface. It is clear therefore that mesh refinement reduces these features. A sensitivity study on the Reynolds number is performed at $Ca = 0.35, \tilde{D}e_d = 0, \tilde{D}e_m = 1.8, \beta_m = 0.68$,

Table 2
Tests for accuracy at $\tilde{D}e_d = 2.6, Ca = 0.35, \hat{t} = 30, \lambda = 1.5, Re = 0.05$

$\Delta x/R_0$	$\Delta t \dot{\gamma}$	D	θ°
1/8	0.0003	0.41	23.0
1/12	0.00014	0.40	23.5
1/16	0.00014	0.39	23.6

The fluid pair is system 1 of Table 1.

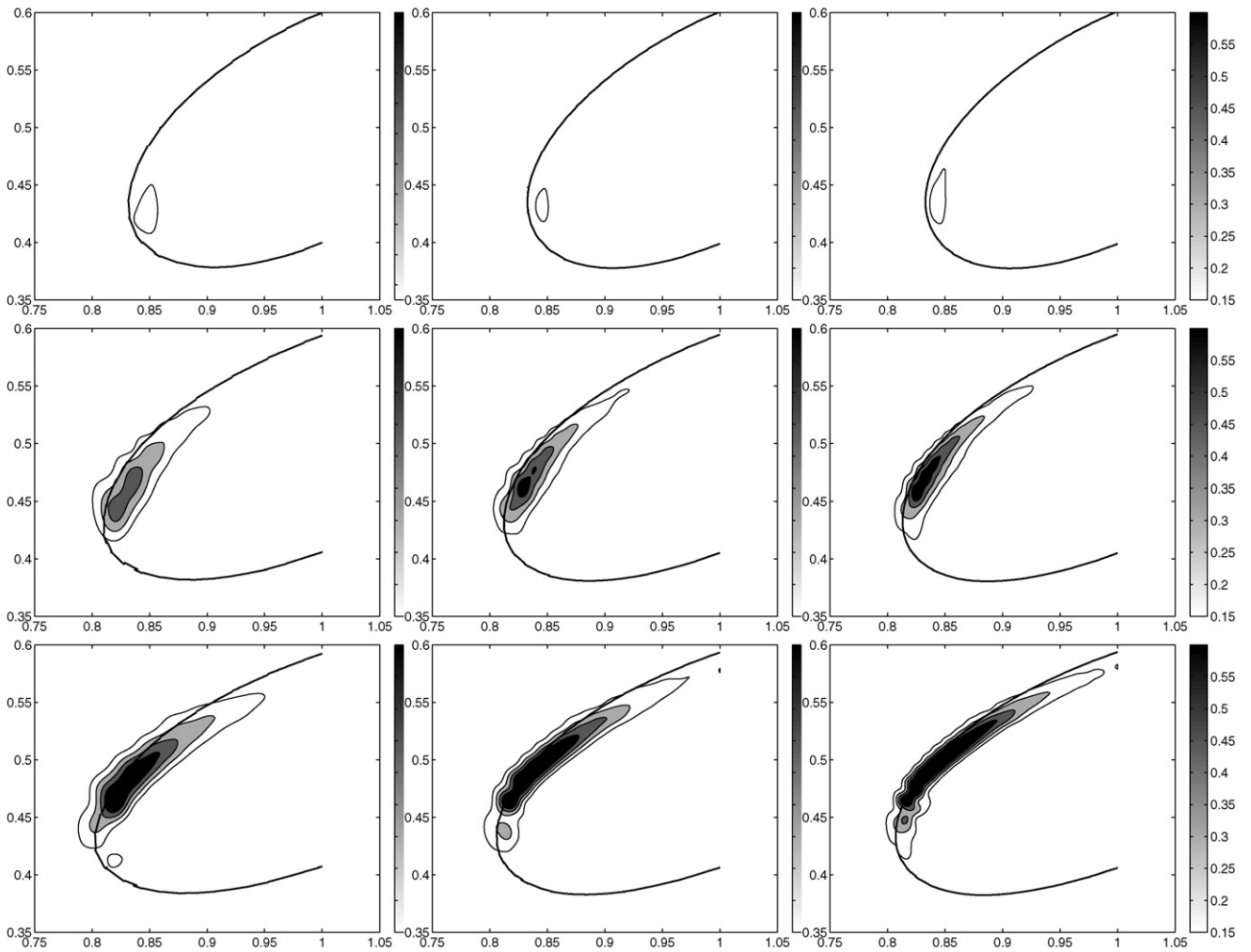


Fig. 2. Contour plots for trace (**T**) for an Oldroyd-B drop in Newtonian matrix, $Ca = 0.35$, $\bar{De}_d = 2.6$, $\lambda = 1.5$, $\hat{t} = 5$ (row 1), 10 (row 2), 15 (row 3); refinement left to right $\Delta x = R_0/8, R_0/12, R_0/16$.

$\lambda = 1.5$, $L_x = 16R_0$, $L_y = 8R_0$, $L_z = 8R_0$, $\Delta x = R_0/12$. The following produce similar results: (i) $Re = 0.05$, $\Delta \hat{t} = 0.00003$, (ii) $Re = 0.01$, $\Delta \hat{t} = 0.00003$, (iii) $Re = 0.05$, $\Delta \hat{t} = 0.000014$, all with CSF, and (iv) $Re = 0.05$, $\Delta \hat{t} = 0.00003$ with PROST. $Re = 0.05$ is chosen as optimal.

3. Materials and experimental methods

Table 1 lists the interfacial tension and viscosity ratio for the droplet–matrix systems used in this study. The first two blends carry a viscoelastic droplet phase; the third blend contains a vis-

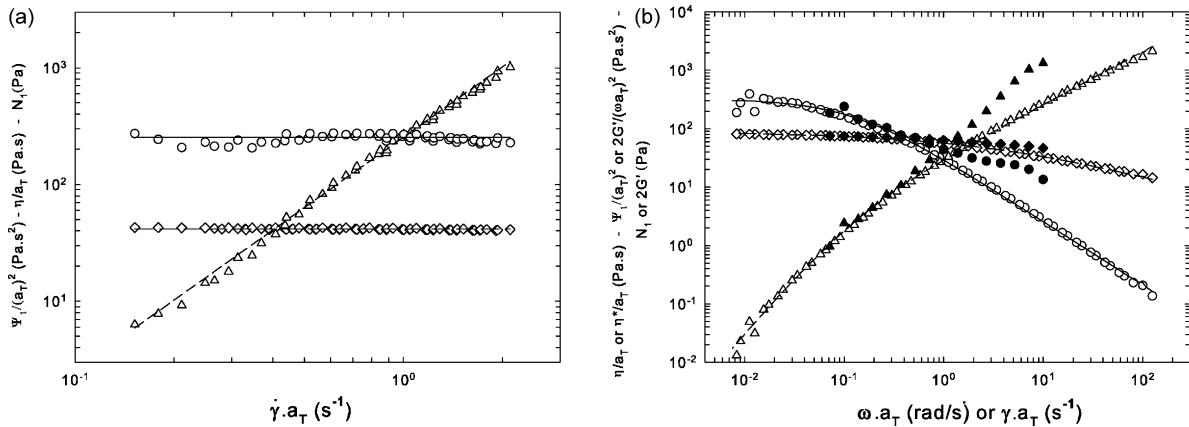


Fig. 3. Rheological characterization of the viscoelastic fluids at a reference temperature of 25°C. (a) PIB Boger fluid BF2. First normal stress difference: Δ , viscosity: \diamond , first normal stress coefficient: \circ ; Lines are the Oldroyd-B model. (b) Branched PDMS BR16. Open symbols are dynamic data, $2G' / (\omega a_T)^2$: \circ , dynamic viscosity: \diamond , $2G''$: Δ ; filled symbols are steady shear data, first normal stress coefficient: \bullet , viscosity: \blacklozenge , first normal stress difference: \blacktriangle ; Lines are the Ellis model.

Table 3
Rheology of the blend components at experimental conditions

Polymer	Grade	Temperature (°C)	η_p (Pa s)	η_s (Pa s)	Ψ_1 (Pa s ²)	τ (s)
PIB	Parapol 1300	25.50	83.5
	Infineum mix	24.45	59.1
	BF2	26.00	12.2	25.7	212	8.7
	BF2	26.40	11.7	24.8	197	8.4
PDMS	Rhodorsil mix 1	26.40	53.8
	Rhodorsil mix 2	25.50	125
	Saturated Rhodorsil	26.00	25.2
	BR16	24.45	88.6 ^a	...	317 ^b	1.8

^a The tabulated viscosity is the zero shear viscosity obtained from a linear fit with Eq. (8), where $k = 0.4992$ and $n = 0.5430$.

^b The tabulated Ψ_1 is the zero shear first normal stress coefficient obtained from a logarithmic fit with Eq. 8, where $k = 9.3550$ and $n = -0.0988$.

coelastic matrix phase; and the fourth one acts as the reference system, containing only Newtonian components.

The viscoelastic material is either a branched polydimethylsiloxane (PDMS) named BR16, or a polyisobuthylene Boger fluid (PIB) named BF2 which is described in detail in [8]. Preparation of the Boger fluid requires the addition of 0.2 wt% of a high molecular weight rubber (Oppanol B200) to a Newtonian PIB (Infineum S1054), which acts as the non-volatile solvent. As Newtonian materials, various mixtures of linear PDMS (Rhodorsil) or PIB (Infineum or Parapol) are used in order to obtain the desired viscosity ratio of 1.5. In addition, the PDMS used as the matrix fluid is saturated with a low molecular weight polyisobuthylene (Indopol H50). This saturation step is necessary to avoid diffusion of PIB molecules, which would lead to droplet shrinkage and a time-dependent interfacial tension [37]. The interfacial tension in Table 1 is measured with two independent methods, which both agree to within experimental error: (i) fitting the droplet deformation at small flow intensity to the second-order theory of Greco [4] and (ii) the pendant drop method.

The rheology of the blend components is discussed in detail in Section 3.A of Ref. [8]. Briefly, all Rhodorsil PDMS mixtures, the Parapol 1300, and the Infineum mixture are Newtonian in the results of this paper. The steady shear rheological data of the PIB Boger fluid at 25 °C is shown in Fig. 3 a. The viscosity and first normal stress coefficient are clearly constants. Thus, the Oldroyd-B constitutive model is appropriate to describe the steady shear rheology, where the solvent viscosity equals that of the non-volatile solvent (Infineum S1054).

Fig. 3 b shows the rheological data of the branched PDMS, clearly displaying shear-thinning behavior. The Cox–Mertz rule is valid at the shear rates applied in the droplet deformation experiments. Hence, to describe the rheology of the branched PDMS, the dynamic data are selected and fitted with an Ellis model [38],

$$\frac{x}{x_0} = \frac{1}{1 + k\omega^{(1-n)}}, \quad (8)$$

where x_0 , k and n are fitting parameters and ω is the oscillation frequency. The resulting rheological parameters of all components at the temperatures used in the droplet deformation experiments are summarized in Table 3.

Droplet deformation experiments with low to moderate Deborah numbers (up to 2) are performed with a counter rotating plate–plate device which is described in detail in Section 3.B of Ref. [8]. The experimental protocol and image analysis are detailed in Section 3.C of Ref. [8]. Digital images are analyzed in the velocity–vorticity plane (top view) and velocity–velocity gradient plane (side view). The major and minor axes of the deformed droplet in the velocity–vorticity plane are obtained by fitting an equivalent ellipse to the drop contour as described in Ref. [39].

Additional droplet deformation experiments are performed with a Linkam CSS 450 shear cell [40]. The optical train consists

of a bright light microscope (Leitz Laborlux 12 Pol S) and a Hamamatsu (Orka 285) digital camera, allowing higher magnifications and better resolution as compared with the counter rotating setup. Hence, smaller droplets can be studied, permitting droplet deformation experiments with Deborah numbers up to 20. Observations are however limited to the velocity–vorticity plane. Moreover, in the Linkam shear cell only the bottom plate rotates, so no stagnation plane exists and the studied droplet moves out of the observation area during flow. Therefore, dilute blends are studied in this apparatus. These blends are obtained by mixing 0.1 wt% of the dispersed phase into the matrix material using a spatula, resulting in countless droplets with a diameter less than 1 μm . The blend is deaerated in a vacuum oven and thereafter pre-sheared in the Linkam apparatus at a shear rate of 0.1 s^{-1} for 48 h. The resulting morphology consists of uniformly distributed droplets with a radius between 10 and 20 μm , for which hydrodynamic and confinement effects (gap of 300 μm) can be excluded. During the droplet deformation experiments, a droplet is examined when entering the field of view, after which the flow is stopped. The droplet relaxes, thereby allowing accurate measurement of its initial radius at rest.

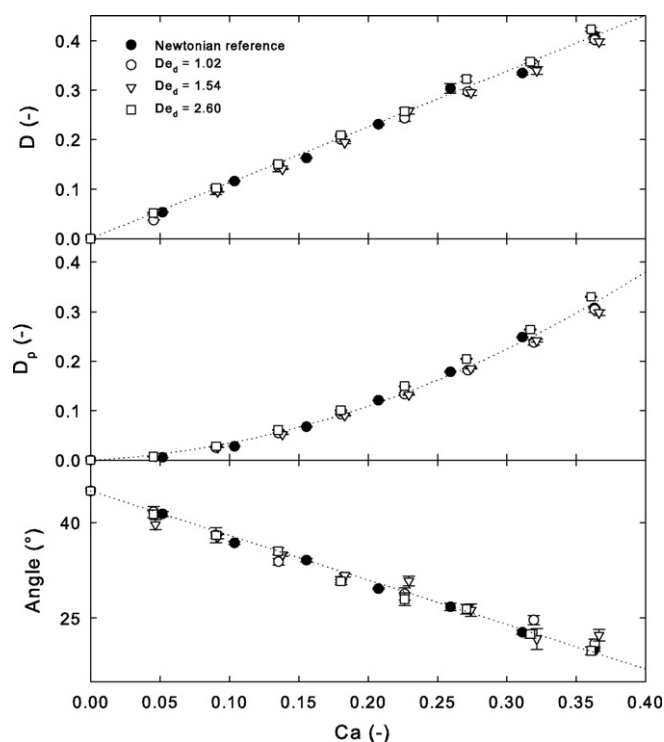


Fig. 4. Steady-state droplet deformations and orientation. Open symbols: Boger fluid droplet–Newtonian matrix system (System 1 of Table 1) at various \overline{De}_d ; filled symbols: Newtonian reference system.

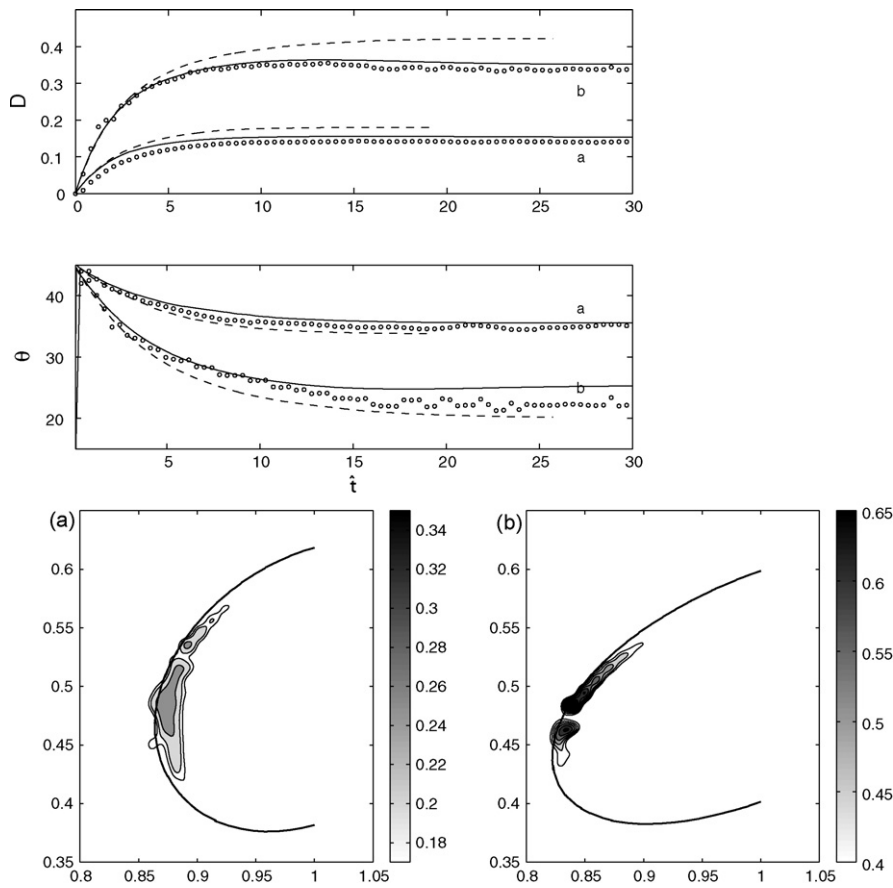


Fig. 5. Side view deformation, 3D VOF-CSF simulation (—) and experimental data (o) at fixed $\tilde{De}_d = 1.54$, for varying $Ca =$ (a) 0.14; (b) 0.32, and Newtonian CSF simulation (---). The contours for trace (T) at stationary states are given.

4. Results and discussion

4.1. Boger fluid droplet system

The effects of droplet viscoelasticity on the droplet deformation and orientation are systematically studied over a wide range of Deborah and capillary numbers and thus contribute to the scarce data on viscoelastic droplet systems. Fig. 4 shows the stationary droplet deformations D and D_p , and orientation of a Boger fluid droplet in a Newtonian matrix (System 1, Table 1). The Newtonian/Newtonian

reference (System 4, Table 1) is also plotted for comparison. The range of Deborah number is achieved by varying the radius of the droplet. The counter-rotating setup was used, yielding the complete 3D picture of the deformed droplet. The figure shows hardly any difference between the elastic droplet system (open symbols) and the Newtonian/Newtonian reference system (filled symbols) at the same capillary number, beyond what one expects as the range of small deformation. Moreover, an increase in the Deborah number, i.e. elasticity, does not result in any change in the steady deformation and orientation, at least within experimental error. Thus, even

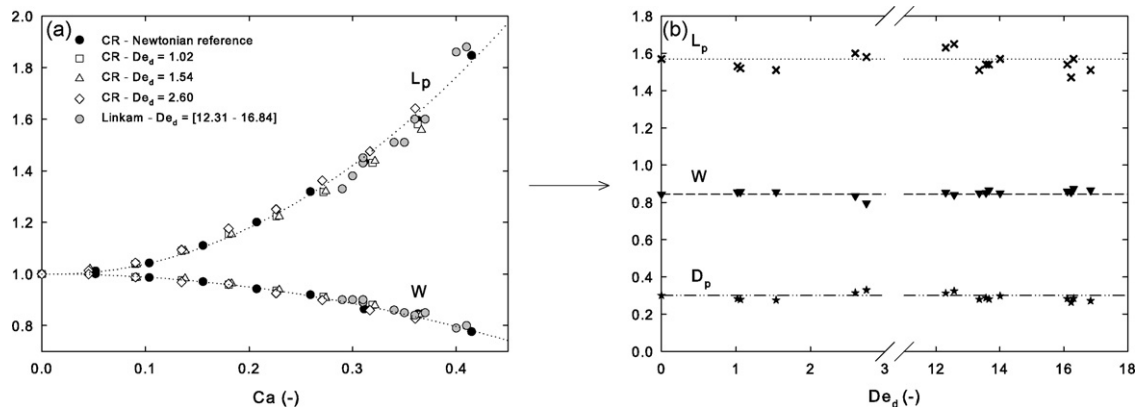


Fig. 6. Steady-state droplet deformation of the Boger fluid droplet system at various \tilde{De}_d numbers. (a) Top view results as a function of the capillary number; open symbols: counter rotating experiments; filled symbols: Newtonian reference system; gray symbols: Linkam experiments. (b) Top view results at fixed $Ca = 0.35$; lines denote Newtonian steady-state deformation.

Table 4

Numerical simulations for steady-state of the elastic drop (system 1, Table 1) at $Ca = 0.35$

\tilde{De}_d	L_p	W	D_p	L	B	D	Angle
1.02	1.51	0.88	0.26	1.63	0.71	0.39	23
2.6	1.53	0.85	0.29	1.65	0.7	0.40	23
4	1.58	0.84	0.31	1.7	0.68	0.43	24
12.31	1.64	0.82	0.33	1.75	0.69	0.43	22

$\tilde{De}_d = 1.02$ ($\Delta x = R_0/8$), 2.6 ($\Delta x = R_0/16$), 4 ($\Delta x = R_0/8$), 12.31 ($\Delta x = R_0/12$).

for Deborah numbers up to almost 3, which represents strong elasticity beyond the small deformation limit, the elastic drop behaves like a Newtonian one.

Numerical simulations and experimental data are compared in Fig. 5 at $\tilde{De}_d = 1.54$ for $Ca = 0.14$ and 0.32. At the lower capillary number, the viscoelastic droplet simulation is similar to the Newtonian droplet simulation. For the higher Ca , the viscoelastic droplet simulation and data show less deformation than the Newtonian simulation. For fixed Deborah number, the magnitude of viscoelastic stress increases with capillary number. The location of the maximum viscoelastic stress migrates to slightly above the drop tip at the back, and slightly below the drop tip at the front when stationary state is reached.

Fig. 6 shows the steady droplet deformation of the Boger fluid droplet system against the capillary number at higher Deborah numbers (\tilde{De}_d up to almost 20), measured with the Linkam shear cell. This setup only allows observations in the velocity–vorticity plane, therefore only information on the axes W and L_p is presented. Fig. 6 also includes the results at smaller \tilde{De}_d , measured with the counter-rotating setup; and the Newtonian reference system, all at a viscosity ratio of 1.5. It is clear that, even at these very large Deb-

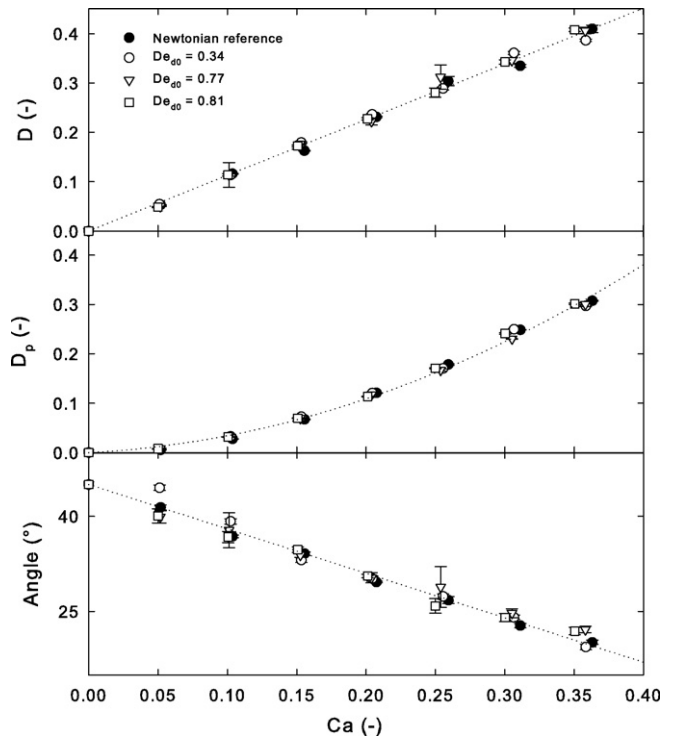


Fig. 8. Steady-state droplet deformation and orientation. Open symbols: Shear-thinning viscoelastic branched fluid droplet–Newtonian matrix system (System 2 of Table 1) at various \tilde{De}_{d0} numbers; filled symbols: Newtonian reference system.

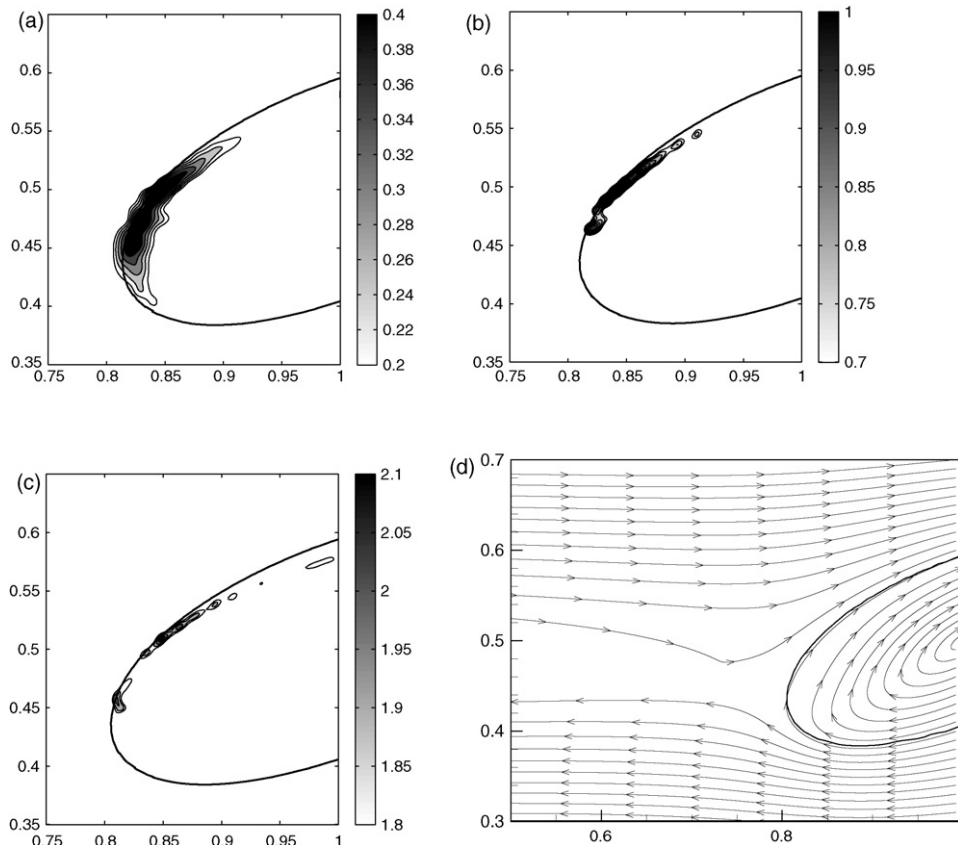


Fig. 7. Stationary state contour plot of trace (T) through the vertical cross-section of the drop at $Ca = 0.35$: (a) $\tilde{De}_d = 1.02$, (b) 2.6, (c) 12.31 and (d) stream lines for $\tilde{De}_d = 12.31$.

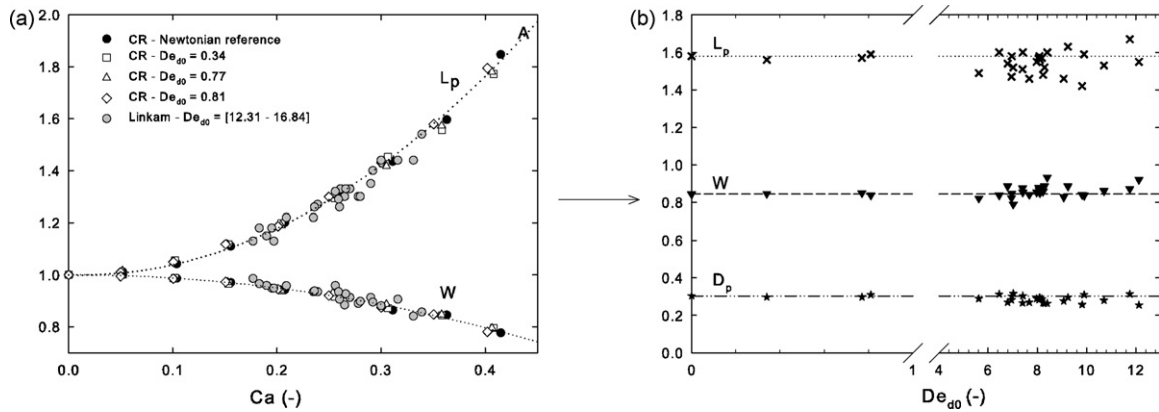


Fig. 9. Steady-state droplet deformation of the shear-thinning viscoelastic branched fluid droplet system at various \tilde{De}_{d0} numbers. (a) Top view results as a function of the capillary number; open symbols: counter rotating experiments; filled symbols: Newtonian reference system; gray symbols: Linkam experiments. (b) Top view results at fixed $Ca = 0.35$; lines denote Newtonian steady-state deformation.

orah numbers, the effect of droplet elasticity is insignificant. One could argue on the basis of Fig. 6 a that at the large \tilde{De}_d numbers the droplet elasticity has the tendency to suppress the droplet deformation by a small amount. But, by presenting the data as shown in Fig. 6 b at a constant capillary number of 0.35, well beyond the range of small deformation, it is obvious that if any effect of droplet elasticity were present on L_p or W , it is within experimental error. This conclusion is even more unmistakable when plotting the deformation parameter D_p (see Fig. 6b), where no effect of droplet elasticity is seen, even at the very high Deborah numbers. These results suggest that the droplet orientation at higher \tilde{De}_d numbers is also hardly affected by droplet elasticity.

Numerical simulations for Fig. 6 are conducted at a fixed $Ca = 0.35$ with varying Deborah numbers. Table 4 shows the steady-state drop diagnostics from VOF-CSF simulations at $Ca = 0.35$, $\tilde{De}_d = 1.02, 2.6, 4, 12.31$. These indicate a slight elongation with increasing \tilde{De}_d .

Fig. 7 shows steady-state contours of trace (\mathbf{T}) for $\tilde{De}_d = 1.02, 2.6, 12.31$. The magnitude of the elastic stresses increases and their location shift to narrower areas along the interface as \tilde{De}_d increases. The velocity fields are similar to the Newtonian reference system, and streamlines are shown for the $\tilde{De}_d = 12.31$. The flow inside the drop is a recirculation, and the accompanying shear rate is different from the imposed shear rate outside the drop and moreover, it is not uniform but depends on the shape of the droplet. In a recirculating flow, the flow does not exhibit much stretching compared with the shear flow in the matrix. Therefore, viscoelastic stresses inside the drop are much smaller than those obtained outside the droplet in a viscoelastic matrix. Thus, the elongational component of the flow is weak, and correspondingly elastic effects; this is reminiscent of other recirculating flows, such as the corner eddies in contraction flow. In particular, the 4:1 contraction flow is known to have corner vortices with only weak elastic stresses [41]. The main difference between these and the drop is that the outer contraction flow determines their sizes, while in the drop system, the size of the recirculation zone is given. At fixed capillary number, the position of maximum viscoelastic stress is seen to move slightly upwards at the back of the drop and also downwards at the front. Since the maxima are not at the drop tips, they promote rotation, and prevent the drop from elongating further.

4.2. Shear-thinning viscoelastic droplet system

In this section, the additional effects of shear-thinning behavior of the droplet fluid are systematically studied at both low and high

shear flow intensities. Fig. 8, for example, shows the steady deformation and orientation for the viscoelastic shear-thinning droplet (system 2 of Table 1) as a function of the capillary and Deborah number. The Newtonian/Newtonian reference system is also plotted for comparison. The applied Deborah numbers are calculated using the zero-shear values of viscosity and first normal stress difference. The steady droplet shapes observed in the velocity–vorticity plane and the velocity–velocity gradient plane do not display any difference with the deformation observed for the Newtonian/Newtonian reference system. Also the orientation of the droplet is similar to that observed for the Newtonian reference system. The drop thus behaves like the Newtonian case, just as the Boger fluid droplet of the previous section, even at capillary numbers beyond the small deformation limit.

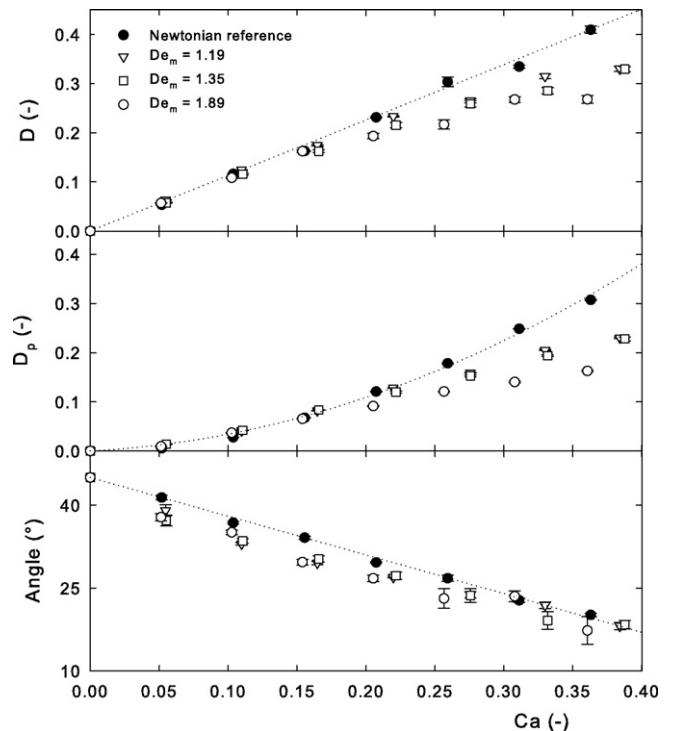


Fig. 10. Steady-state droplet deformation and orientation. Open symbols: Newtonian droplet–Boger fluid matrix system (System 3 of Table 1) at various \tilde{De}_m numbers; filled symbols: Newtonian reference system.

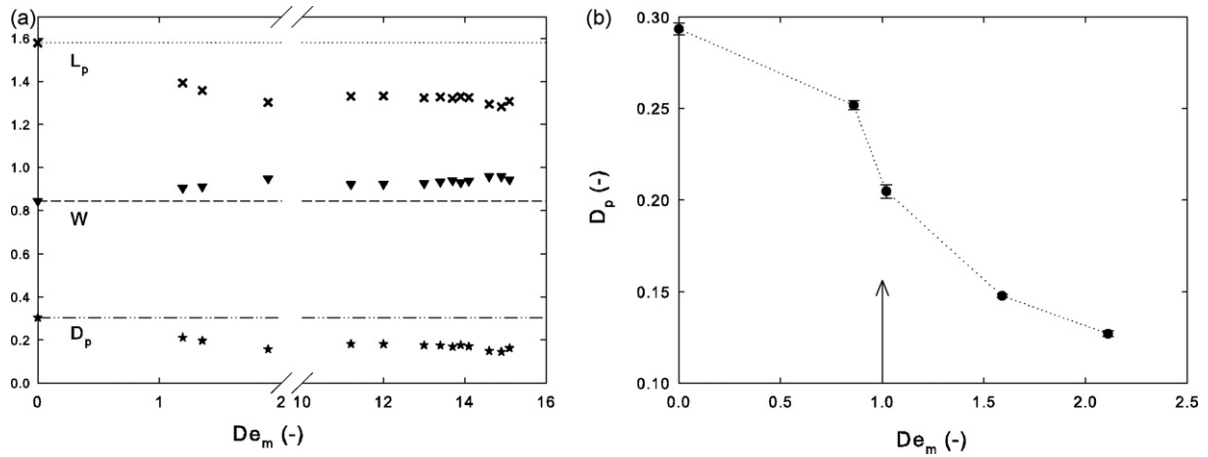


Fig. 11. Steady-state droplet deformation of Boger fluid matrix system at various \tilde{De}_m numbers. (a) Steady droplet deformation observed in the velocity–vorticity plane at $Ca = 0.35$, lines denote Newtonian steady-state deformation. (b) BF2 data taken from [8] at $Ca = 0.35$ and viscosity ratio 0.75.

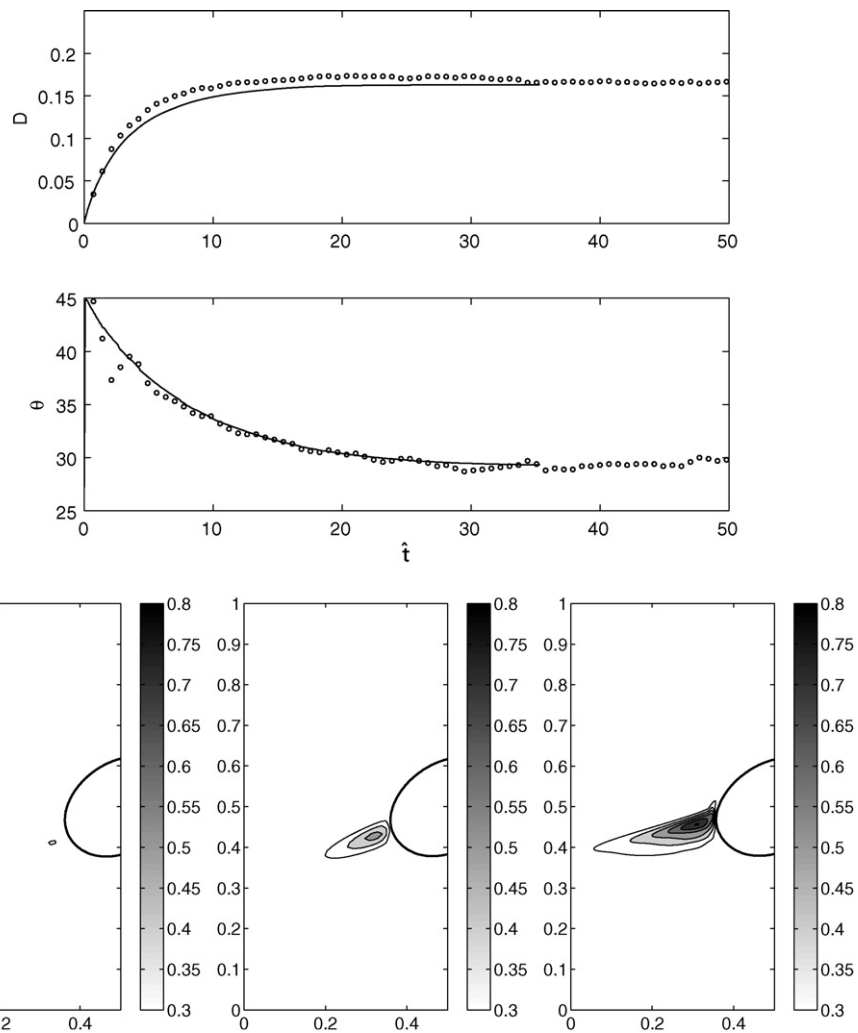


Fig. 12. Newtonian drop in an Oldroyd-B matrix with $Ca = 0.154$, $\tilde{De}_m = 1.89$, $\lambda = 1.5$, $\beta_m = 0.68$; o, experimental data; —, VOF-CSF simulation. Drop shapes and viscoelastic stress levels through the vertical cross-section at drop center are shown at $\hat{t} = 10, 15, 30$.

Fig. 9 a shows the steady droplet deformation of the viscoelastic shear-thinning droplet, observed in the velocity–vorticity plane at very high Deborah numbers, i.e. smaller droplets. The data are obtained with the Linkam shear cell, studying individual droplets. The steady droplet deformations, measured with the counter rotating setup are also displayed. It is shown that even at very large Deborah numbers ($\tilde{D}e_{d0}$ up to 12), or equivalent imposed shear rates up to 3 s^{-1} , the effect of droplet elasticity and shear-thinning behavior is insignificant, although somewhat more scatter is observed in the Linkam experiments. This becomes more obvious if the results are plotted versus the Deborah number, as shown in Fig. 9 b at a constant capillary number of 0.35. The lines represent the corresponding Newtonian steady deformation. It is

obvious that if any effect of droplet elasticity and shear-thinning behavior would be present, it is small and within experimental error.

As in the previous section (e.g., Fig. 5), numerical simulations with the Oldroyd-B model at $\beta_{d0} = 0.6$ produce similar droplet history as the Newtonian case. Introducing the shear-thinning by means of a Giesekus model, thereby resembling the rheology fitted with the Ellis model as exactly as possible, does not have a pronounced effect on the resulting steady deformation and orientation. Therefore, the numerical results are omitted here since they mirror those of the previous section. This result is however not surprising, the shear rate inside the droplet is much smaller than the imposed shear rate, and the elastic stresses

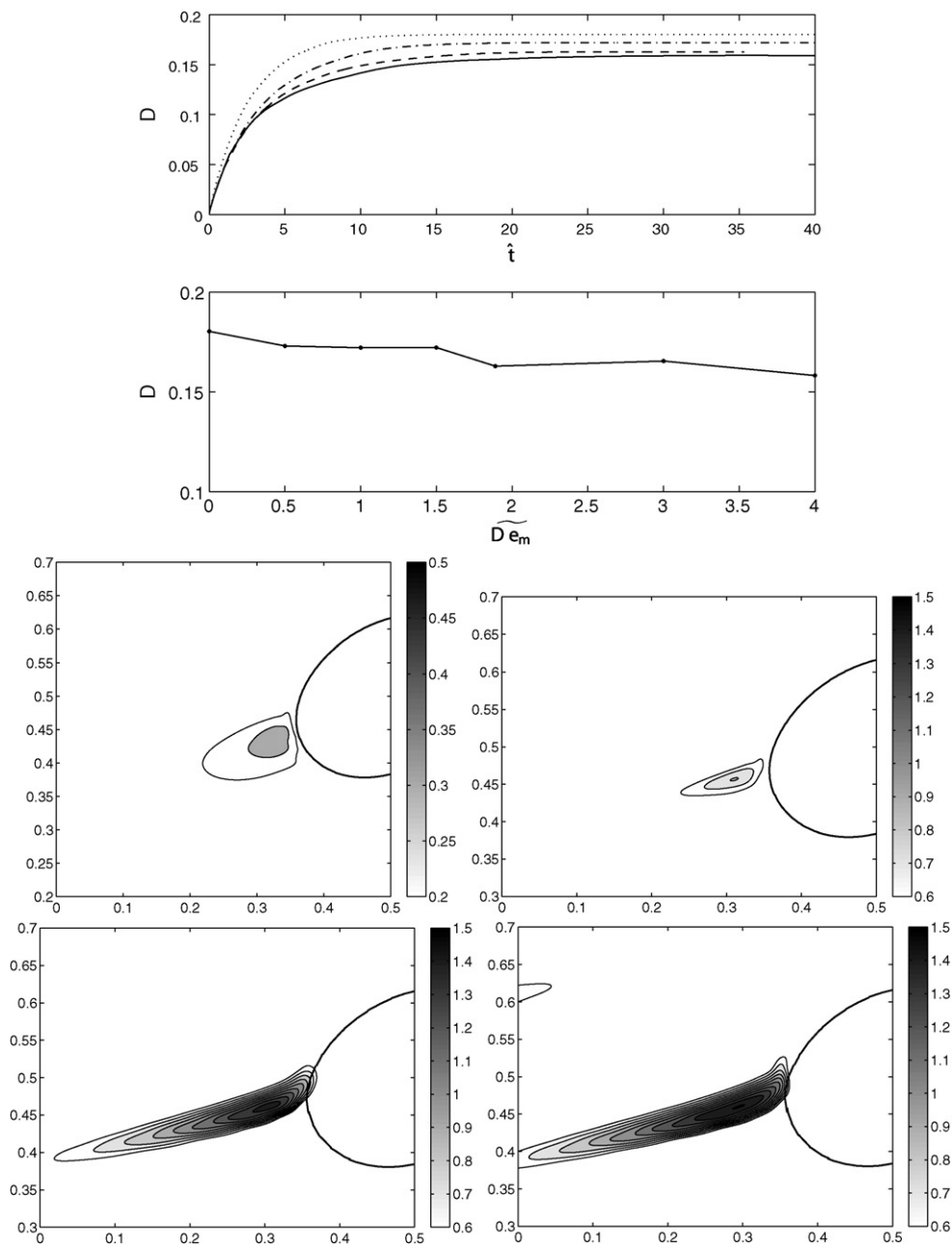


Fig. 13. Newtonian drop in BF2 system, modelled with Oldroyd-B. $Ca = 0.154$. The temporal evolution of deformation for $\tilde{D}e_m = 0$ (…), 1 (– · –), 1.89 (– –), 4 (–), together with the stationary values of deformation D vs. $\tilde{D}e_m$. Contours of trace (\mathbf{T}) for $\tilde{D}e_m = 1, 1.89, 4, 6$ at $\hat{t} = 30$.

generated by the recirculation inside the droplet are small, similar to what is shown for the Boger fluid droplet system (see Fig. 7).

4.3. Boger fluid matrix system

In Fig. 10, the steady droplet deformation and orientation for a Newtonian drop–Boger fluid matrix (system 3 of Table 1) are plotted as a function of capillary and Deborah number, together with the Newtonian reference system. This clearly shows two pri-

mary effects of introducing matrix elasticity, comparable to the results at other viscosity ratios [7,8]: (i) to promote drop orientation towards the flow direction even at low flow intensities, and (ii) to suppress droplet deformation at higher capillary numbers. These and previous data, do however not allow validation of the non-monotonous dependency of the stationary droplet deformation on matrix viscoelasticity as obtained with the 2D simulations by Yue et al. [22]. Therefore, the stationary droplet deformation and orientation at higher Deborah numbers are addressed in Fig. 11 a.

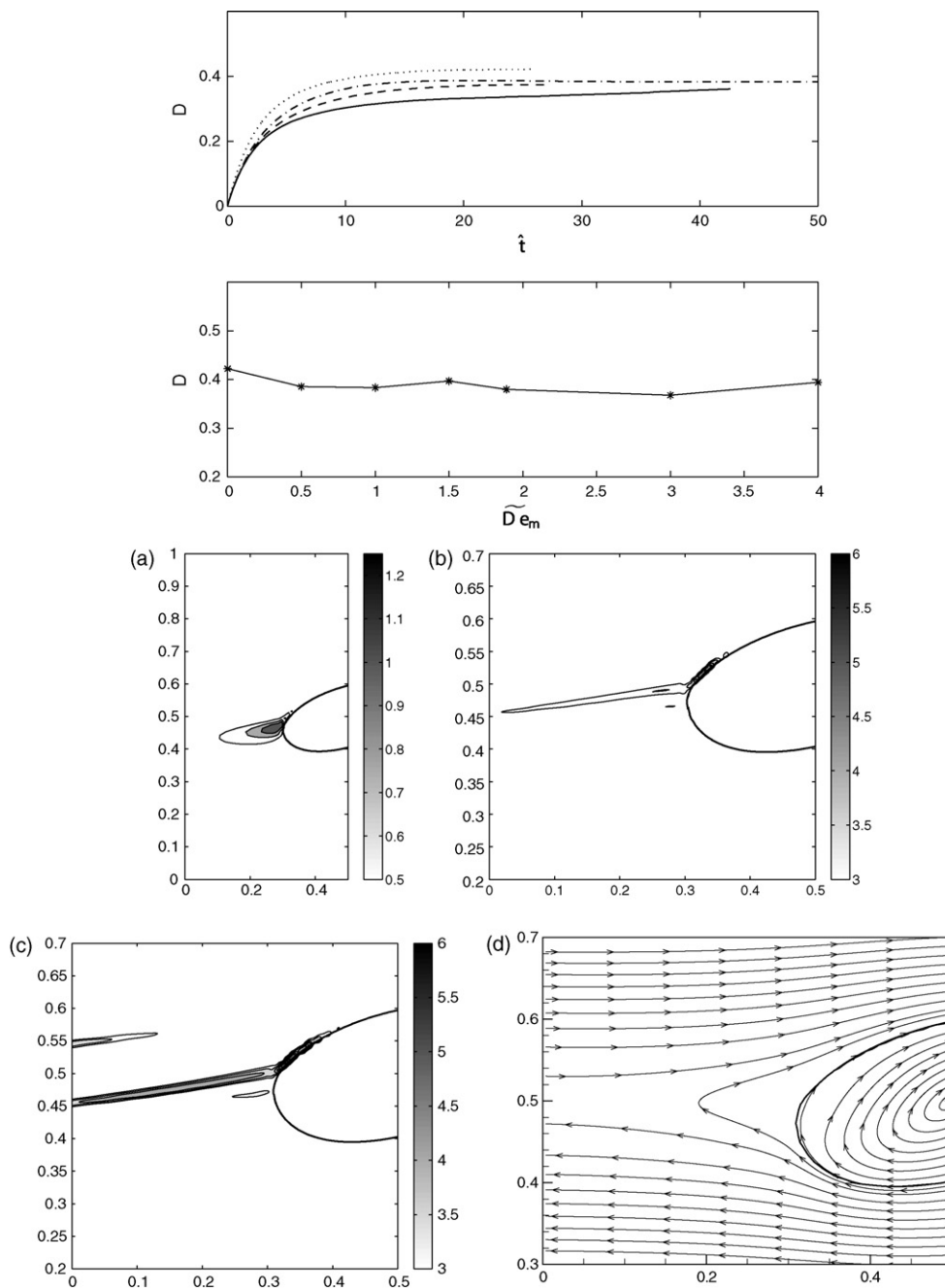


Fig. 14. Newtonian drop in BF2 system, $Ca = 0.35$. The temporal evolution of deformation for $\tilde{D}e_m = 0$ (· · ·), 1 (– · –), 1.89 (– –), 4 (–), with the Oldroyd-B model. The lower plot shows $\hat{t} = 40$ values of deformation D vs. $\tilde{D}e_m$. Viscoelastic stress contour plots in the x - z plane for $\tilde{D}e_m = 1$, (a) at $\hat{t} = 40$, and for $\tilde{D}e_m = 3$ (b), 4 (c), and stream lines for $\tilde{D}e_m = 4$ (d) at $\hat{t} = 30$.

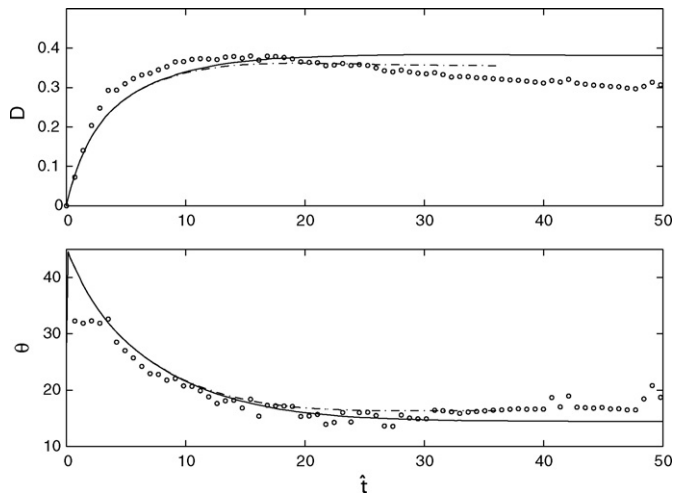


Fig. 15. Newtonian drop in BF2 matrix with $Ca = 0.36$, $\tilde{De}_m = 1.89$, $\lambda = 1.5$, $\beta_m = 0.68$. Experimental data \circ ; 3D Oldroyd-B model $-$; Giesekus model with $\hat{\kappa}_m = 0.01$ $- -$.

Fig. 11 a shows the steady droplet deformation of the Boger fluid matrix system, observed in the velocity–vorticity plane, plotted as a function of the Deborah number (up to 16) at $Ca = 0.35$. It is shown that at $\tilde{De}_m \approx 2$, the effect of matrix elasticity saturates. The dependency at lower Deborah number (< 2) is similar to that obtained for the BF2 matrix system with a viscosity ratio of 0.75, studied in Verhulst et al. [8], and replotted here in figure 11 b. Both experiments thus qualitatively yield the same results. At $\tilde{De}_m < 2$, a decrease in droplet size, or equivalently, an increase in the applied \tilde{De}_m , results in a decrease of the steady droplet deformation. A sigmoidal dependency on the Deborah number is seen with an inflexion point around $\tilde{De}_m \approx 1$; the point where non-Newtonian effects are expected to become visible [4].

These experimentally observed trends are at least qualitatively predicted by the various phenomenological models presented in literature [8–11], although they are predicting a monotonous decrease of the droplet deformation with increasing \tilde{De}_m . Hence, the quantitative prediction of these models at high capillary numbers is less satisfying. Verhulst et al. [8] attribute this to the simplicity of the rheological model used by [10]. Hence, in the numerical simulations, the Oldroyd-B model is chosen to describe the rheology of the Boger fluid. Numerical simulations are conducted at $Ca = 0.154, 0.35$, or 0.361 , and compared with the data of Figs. 10 and 11 a.

Simulations at low capillary number agree quite well with experimental data, as exemplified by Fig. 12 at $Ca = 0.154$ and $\tilde{De}_m = 1.89$, with $\lambda = 1.5$, $\beta_m = 0.68$. Both deformation and angle of inclination are shown to be closely predicted. Contours of trace (\mathbf{T}) at $\hat{t} = 10, 15, 30$ are also shown in the figure. As time progresses, the area of largest viscoelastic stress moves from the drop tip slightly upwards. In Fig. 13, simulations with $Ca = 0.154$, and \tilde{De}_m increasing from 0 to 4, are shown because the experimental data show saturation in D as the Deborah number increases. For higher Deborah numbers, more mesh refinement is required to capture the high gradient in viscoelastic stress at drop tips, and the initial transient takes longer. Deformation vs. \hat{t} is shown in the upper plot, from which $\hat{t} = 40$ is used to plot the stationary D vs. \tilde{De}_m . Numerical results in Fig. 13 show little change in the stationary

deformation between $\tilde{De}_m = 0.5$ and 1.5 , and then a decrease. Contours of trace(\mathbf{T}) are shown at $\hat{t} = 30$, which is close to stationary state. Due to spatial periodicity in the x -direction, contours may enter from the left boundary, as for the case $\tilde{De}_m = 6$.

At the higher capillary number $Ca = 0.35$, simulations with the Oldroyd-B model are shown in Fig. 14. The upper plot shows the evolution of deformation for $\tilde{De}_m = 0(\dots) 1$ ($- \cdot -$), 1.89 ($- -$), 4 ($-$). The transients take longer to settle with increasing Deborah number and $\tilde{De}_m = 4$ is still slightly elongating in the figure. In the lower figure, the $\hat{t} = 40$ deformation values vs. \tilde{De}_m are plotted. These are roughly stationary states. The 2D counterpart of this study is in Fig. 1 of [22]: non-monotonic dependence of steady-state deformation as a function of the Deborah number for capillary number 0.1 and 0.2. Their deformation at $Ca = 0.1$ hits a minimum value of $D = 0.103$ at Deborah number 0.5 and then increases to $D = 0.122$ at Deborah number 2. At $Ca = 0.2$, their minimum shifts to Deborah number 0.8. The 3D calculations are qualitatively different from these. The 2D case is that of an infinitely long cylindrical interface, and differs from 3D results at higher deformations (see Fig. 1 of [42] for another example). The contours for trace (\mathbf{T}) are shown at $\tilde{De}_m = 1, 3, 4$ at fixed $\hat{t} = 40$. The location of the maxima lie slightly above the drop tip at the back of the drop rather than at the drop tips, directly at the interface. The streamlines are shown in the x – z cross-section for $\tilde{De}_m = 4$, and the dividing streamline appears to correspond with the high viscoelastic stresses that come off of the drop in a narrow region.

Fig. 15 shows temporal evolution for the particular case of $Ca = 0.35$, $\tilde{De}_m = 1.89$, for experimental data (\circ) against the 3D Oldroyd B model ($-$) and the Giesekus model with $\hat{\kappa}_m = 0.01$. There is a slight decay in deformation in the Oldroyd B simulation for large time, but it essentially saturates to a constant value of deformation and angle. The Giesekus model displays more damping in the deformation and gives a better fit to the data. The data shows additional damping as time progresses, which may reflect the presence of more than one relaxation time. The effect of changing the retardation parameter in the 3D simulations is that increasing from $\beta_m = 0.26$ to $\beta_m = 0.8$ decreases the maximum deformation. This provides a check that the value $\beta_m = 0.68$ deduced from Table 3 is consistent.

The introduction of shear-thinning in the 3D simulation relieves the overall stress as shown in Fig. 16. The left hand column shows the viscoelastic stress growing in intensity, while the addition of $\hat{\kappa}_m = 0.01$ is shown on the right at the corresponding times. The effect of introducing the Giesekus parameter is a slight decrease in the stationary state deformation, and slight increase in the angle of inclination, both of which improve the agreement with the experimental data. However, both settle to constant values rather than the prolonged decay in deformation observed in the data, which may be due to multiple relaxation times. We therefore develop the 5-mode Giesekus model in Appendix A that more accurately describes the linear viscoelasticity, the steady shear rheology, and steady and transient extensional rheology. It is evident that the presence of the long relaxation time for fluid BF2 explains the decay in the experimental data. The 5-mode model is also used in the second part of this work when describing drop relaxation [42]. The single mode rheological characterization from [43] has been used throughout this paper in the numerical simulations. (Note that the simulations of [26] at the higher capillary numbers with the Oldroyd-B model over-predicts the viscoelastic stresses, and they use a Giesekus model in order to compare with experimental data. In fact, this is due to an error in their code which has been corrected in this paper.)

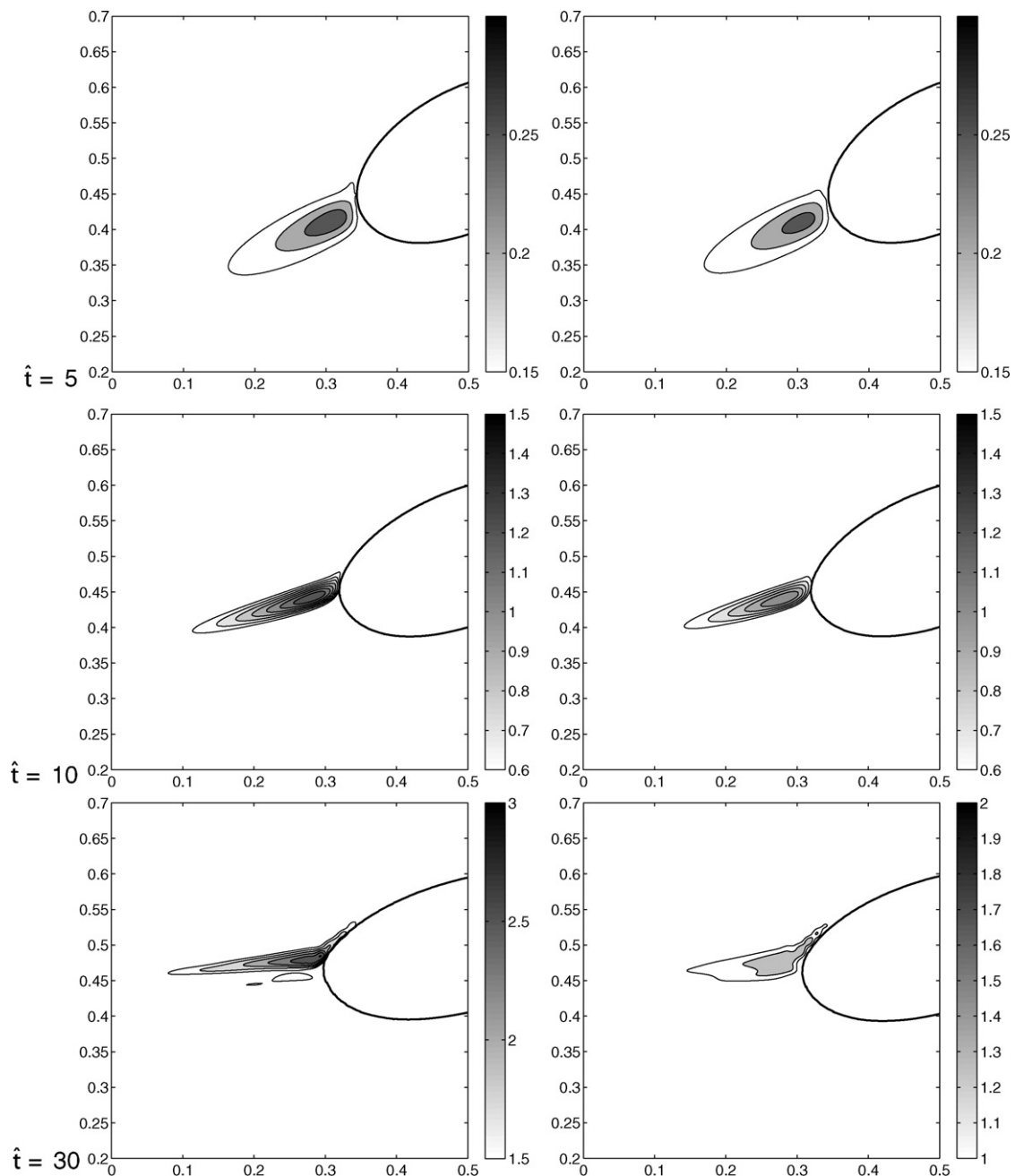


Fig. 16. Contours for trace (T) through the vertical cross-section of a drop for Fig. 15. Newtonian drop in an Oldroyd-B fluid (left) with $Ca = 0.361$, $\bar{D}e_m = 1.89$, $\lambda = 1.5$, $\beta_m = 0.68$, and Giesekus model with $\hat{\kappa}_m = 0.01$ (right) at $\hat{t} = 5, 10, 30$.

5. Conclusion

The influence of matrix and droplet viscoelasticity on the steady deformation and orientation of a single droplet subjected to a homogeneous shear flow is investigated microscopically. The viscosity ratio is 1.5 and we focus on capillary numbers around 0.15 and 0.35, outside the range of small deformation asymptotics. Droplet viscoelasticity has hardly any effect on the steady droplet deformation and orientation, even at moderate to high capillary and Deborah numbers. Matrix elasticity, on the other hand, significantly suppresses droplet deformation and promotes droplet orientation, two effects that saturate at high Deborah numbers. This corresponds to decreasing the droplet radius under the same physical conditions. These experimental results are in quantitative agree-

ment with 3D simulations performed with the Oldroyd-B model; accurate results for the higher capillary number are obtained numerically for the first time. The 3D simulations also show for the first time that the stationary value of deformation saturates at higher matrix Deborah numbers, which is also observed in the experimental data. The introduction of some shear-thinning in the matrix fluid by means of a Giesekus model yields the trend that the deformation is lower and the angle is higher, both of which are in the direction of the data. Additionally, the experimental data show a greater decay in stationary state deformation over a longer time scale than is described by the rheological models used in the numerical simulations. This is reconciled by the presence of a mode with a longer relaxation time in the 5-mode Giesekus model described in Appendix A (Table 5).

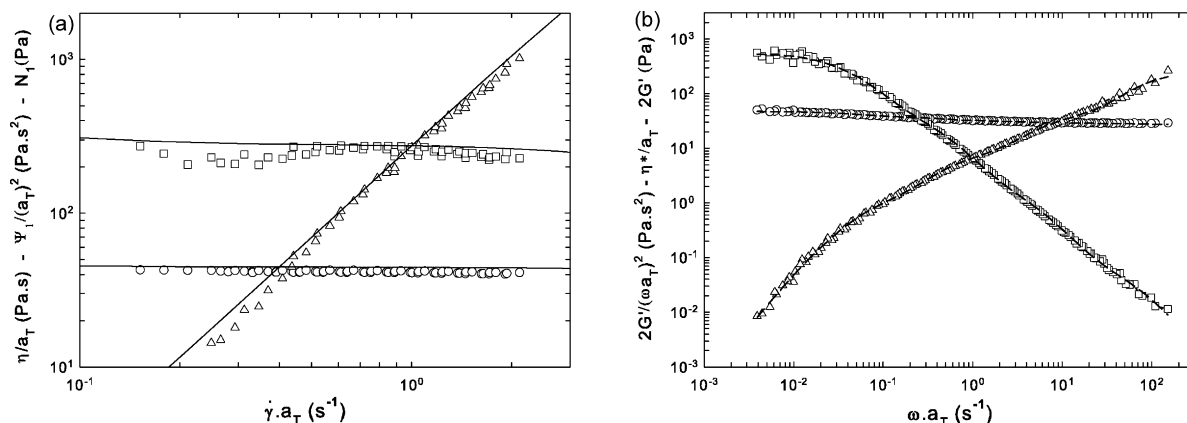


Fig. A.1. Rheological characterization of BF2. (a) Steady shear rheology: first normal stress difference Δ , viscosity η , first normal stress coefficient Ψ_1 . (b) Linear viscoelasticity: $2G''/(\omega a_T)^2$, dynamic viscosity η^* , $2G'$. Lines are the 5 mode Giesekus model.

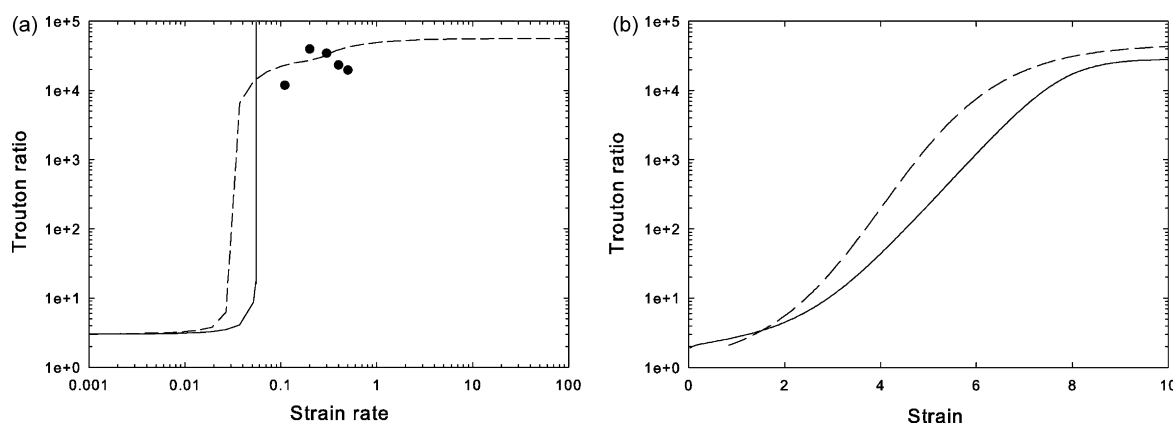


Fig. A.2. Rheological characterization of BF2. (a) Steady Trouton ratio. Symbols: experimental data, line: Oldroyd-B model, dashed line: 5 mode giesekus model. (b) Transient Trouton ratio at strain rate of 0.3 s^{-1} . Dashed line: experimental data, line: 5 mode Giesekus model.

Acknowledgements

This research is supported by NSF-DMS-0456086, NCSA CTS060022, GOA 03/06 and FWO-Vlaanderen for a fellowship for Ruth Cardinaels. The authors would like to thank Prof. Sridhar of Monash University for measuring the extensional rheology of our samples, and Pascal Gillioen & Dr. Jorg Lauger of Anton Paar for their help with the counter rotating device.

Appendix A

A 5-mode Giesekus model is proposed to describe the rheology of the Boger fluid BF2. It describes the linear viscoelasticity, the steady shear rheology, and steady and transient extensional rheology, as demonstrated in Figs. A.1 and A.2. All data are temperature

Table 5
Giesekus description with 5 relaxation modes of the BF2 fluid

Mode	τ (s)	η_p (Pa s)	$\hat{\kappa}$
1	49	2.66	0.2
2	16.9	7.43	0.00001
3	2.03	5.82	0.00001
4	0.187	2.69	0.2
5	0.0131	1.39	0.2
Solvent	–	27.2	–

super-positioned with a reference temperature of 25°C . The shift-factors a_T at a temperature of 26°C and 26.4°C are 0.915 and 0.882.

The longest relaxation time is obtained from capillary break-up measurements using a Caber device. The four additional relaxation times and their corresponding partial viscosities are obtained from fitting the linear viscoelasticity with 5 Maxwell modes, as described by Quinzani et al. [44]. The $\hat{\kappa}$ -values are obtained from fitting the steady shear data. The resulting 5 relaxation times and their corresponding partial viscosities and $\hat{\kappa}$ -values; and the solvent viscosity are given in Table 5.

References

- [1] R.G. Larson, The Structure and Rheology of Complex Fluids, Oxford University Press, 1999.
- [2] L.A. Utracki, Polymer Alloys and Blends, Hanser Munich, 1989.
- [3] S. Guido, F. Greco, Dynamics of a liquid drop in a flowing immiscible liquid, in: D.M. Binding, K. Walters (Eds.), Rheology Reviews, British Society of Rheology, 2004, pp. 99–142.
- [4] F. Greco, Drop deformation for non-Newtonian fluids in slow flows, J. Non-Newtonian Fluid Mech. (2002) 111–131.
- [5] W. Yu, M. Bousmina, C. Zhou, C.L. Tucker, Theory for drop deformation in viscoelastic systems, J. Rheol. 48 (2) (2004) 417–438.
- [6] S. Guido, M. Simeone, F. Greco, Effects of matrix viscoelasticity on drop deformation in dilute polymer blends under slow shear flow, Polymer 44 (2003) 467–471.
- [7] S. Guido, M. Simeone, F. Greco, Deformation of a Newtonian drop in a viscoelastic matrix under steady shear flow. Experimental validation of slow flow theory, J. Non-Newtonian Fluid Mech. 114 (2003) 65–82.

- [8] K. Verhulst, P. Moldenaers, M. Minale, Drop shape dynamics of a Newtonian drop in a non-Newtonian matrix during transient and steady shear flow, *J. Rheol.* 51 (2007) 261–273.
- [9] P.L. Maffettone, F. Greco, Ellipsoidal drop model for single drop dynamics with Non-Newtonian fluids, *J. Rheol.* 48 (2004) 83–100.
- [10] M. Minale, Deformation of a non-Newtonian ellipsoidal drop in a non-Newtonian matrix: extension of Maffettone–Minale model, *J. Non-Newtonian Fluid Mech.* 123 (2004) 151–160.
- [11] W. Yu, C. Zhou, M. Bousmina, Theory of morphology evolution in mixtures of viscoelastic immiscible components, *J. Rheol.* 49 (2005) 215–236.
- [12] P.L. Maffettone, F. Greco, M. Simeone, S. Guido, Analysis of start-up dynamics of a single drop through an ellipsoidal drop model for non-Newtonian fluids, *J. Non-Newtonian Fluid Mech.* 126 (2005) 145–151.
- [13] V. Sibillo, S. Guido, F. Greco, P.L. Maffettone, Single drop dynamics under shearing flow in systems with a viscoelastic phase, in: *Times of Polymers, Macromolecular Symposium* 228, Wiley, 2005, pp. 31–39.
- [14] V. Sibillo, M. Simeone, S. Guido, F. Greco, P.L. Maffettone, Start-up and retraction dynamics of a Newtonian drop in a viscoelastic matrix under simple shear flow, *J. Non-Newtonian Fluid Mech.* 134 (2006) 27–32.
- [15] D.C. Trethewey, L.G. Leal, Deformation and relaxation of Newtonian drops in planar extensional flow of a Boger fluid, *J. Non-Newtonian Fluid Mech.* 99 (2001) 81–108.
- [16] F. Mighri, A. Ajji, P.J. Carreau, Influence of elastic properties on drop deformation in elongational flow, *J. Rheol.* 41 (5) (1997) 1183–1201.
- [17] H.B. Chin, C.D. Han, Studies on droplet deformation and breakup. I. Droplet deformation in extensional flow, *J. Rheol.* 23 (5) (1979) 557–590.
- [18] W.J. Milliken, L.G. Leal, Deformation and breakup of viscoelastic drops in planar extensional flows, *J. Non-Newtonian Fluid Mech.* 40 (1991) 355–379.
- [19] H. Vanoene, Modes of dispersion of viscoelastic fluids in flow, *J. Colloid Interface Sci.* 40 (3) (1972) 448–467.
- [20] J.J. Elmendorp, R.J. Maalcke, A study on polymer blending microrheology: Part 1, *Polym. Eng. Sci.* 25 (1985) 1041–1047.
- [21] F. Mighri, P.J. Carreau, Influence of elastic properties on drop deformation and breakup in shear flow, *J. Rheol.* 42 (1998) 1477–1490.
- [22] P. Yue, J.J. Feng, C. Liu, Viscoelastic effects on drop deformation in steady shear, *J. Fluid Mech.* 540 (2005) 427–437.
- [23] W. Lerdwijitjarud, R.G. Larson, A. Sirivat, M.J. Solomon, Influence of weak elasticity of dispersed phase on droplet behavior in sheared polybutadiene/poly(dimethyl siloxane) blends, *J. Rheol.* 47 (1) (2003) 37–58.
- [24] W. Lerdwijitjarud, A. Sirivat, R.G. Larson, Influence of dispersed-phase elasticity on steady-state deformation and breakup of droplets in simple shearing flow of immiscible polymer blends, *J. Rheol.* 48 (4) (2004) 843–862.
- [25] N. Aggarwal, K. Sarkar, Deformation and breakup of a viscoelastic drop in a Newtonian matrix under steady shear, *J. Fluid Mech.* 584 (2007) 1–21.
- [26] D. Khismatullin, Y. Renardy, M. Renardy, Development and implementation of VOF-PROST for 3d viscoelastic liquid–liquid simulations, *J. Non-Newtonian Fluid Mech.* 140 (2006) 120–131.
- [27] S.B. Pillapakam, P. Singh, A level-set method for computing solutions to viscoelastic two-phase flow, *J. Comp. Phys.* 174 (2001) 552–578.
- [28] T. Chinyoka, Y. Renardy, M. Renardy, D.B. Khismatullin, Two-dimensional study of drop deformation under simple shear for Oldroyd-B liquids, *J. Non-Newtonian Fluid Mech.* 130 (2005) 45–56.
- [29] H.K. Ganpule, B. Khomami, A theoretical investigation of interfacial instabilities in the three layer superposed channel flow of viscoelastic fluids, *J. Non-Newtonian Fluid Mech.* 79 (1998) 315–360.
- [30] Y. Renardy, M. Renardy, Instability due to second normal stress jump in two-layer shear flow of the Giesekus fluid, *J. Non-Newtonian Fluid Mech.* 81 (1999) 215–234.
- [31] J. Li, Y. Renardy, M. Renardy, Numerical simulation of breakup of a viscous drop in simple shear flow through a volume-of-fluid method, *Phys. Fluids* 12 (2000) 269–282.
- [32] Y. Renardy, M. Renardy, PROST: a parabolic reconstruction of surface tension for the volume-of-fluid method, *J. Comp. Phys.* 183 (2002) 400–421.
- [33] Y. Renardy, J. Li, Parallelized simulations of two-fluid dispersions, *SIAM News* 33 (10) (2000) 1.
- [34] A. Vananroye, P. Van Puyvelde, P. Moldenaers, Effect of confinement on droplet breakup in sheared emulsions, *Langmuir* 22 (2006) 3972–3974.
- [35] A. Vananroye, P. Van Puyvelde, P. Moldenaers, Effect of confinement on the steady-state behavior of single droplets during shear flow, *J. Rheol.* 51 (1) (2007) 139–153.
- [36] V. Cristini, J. Blawdziewicz, M. Loewenberg, Drop breakup in three-dimensional viscous flows, *Phys. fluids* 10 (8) (1998) 1781–1783.
- [37] S. Guido, M. Simeone, M. Villone, Diffusion effects on the interfacial tension of immiscible polymer blends, *Rheol. Acta* 38 (1999) 287–296.
- [38] C.W. Macosko, *Rheology Principles, Measurements and Applications*, VCH Publishers, Inc., New York, 1994.
- [39] S. Guido, M. Villone, Three-dimensional shape of a drop under simple shear flow, *J. Rheol.* 42 (1998) 395–415.
- [40] A. Vananroye, P. Van Puyvelde, P. Moldenaers, Structure development in confined polymer blends: steady-state shear flow and relaxation, *Langmuir* 22 (2006) 2273–2280.
- [41] P. Wapperom, M.F. Webster, Simulation for viscoelastic flow by a finite volume/element method, *Comput. Appl. Mech. Eng.* 180 (1999) 281–304.
- [42] K. Verhulst, R. Cardinaels, P. Moldenaers, S. Afkhami, Y. Renardy, Influence of viscoelasticity on drop deformation and orientation in shear flow. Part 2. Dynamics, *J. Non-Newtonian Fluid Mech.*, submitted for publication.
- [43] K. Verhulst, P. Moldenaers, M. Minale, Drop shape dynamics of a Newtonian drop in a non-Newtonian matrix during transient and steady shear flow, *J. Rheol.* 51 (2007) 261–273.
- [44] L.M. Quinzani, G.H. McKinley, R.A. Brown, R.C. Armstrong, Modeling the rheology of polyisobutylene solutions, *J. Rheol.* 34 (5) (1990) 705–748.